Evolution of elastic x-ray scattering in laser-shocked warm dense lithium

N. L. Kugland,[1,2] G. Gregori,[3] S. Bandyopadhyay,[4] C. M. Brenner,[5,4] C. R. D. Brown,[6,7] C. Constantin,[1]
S. H. Glenzer,[2] F. Y. Khattak,[8] A. L. Kritcher,[9,2] C. Niemann,[1,2] A. Otten,[10] J. Pasley,[11,4] A. Pelka,[10]
M. Roth,[10] C. Spindloe,[4] and D. Riley[12]

[1]*Physics Department, University of California–Los Angeles, Los Angeles, California 90095, USA*
[2]*Lawrence Livermore National Laboratory, Livermore, California 94550, USA*
[3]*Clarendon Laboratory, University of Oxford, Parks Road, Oxford OX1 3PU, United Kingdom*
[4]*CLF, Rutherford Appleton Laboratory, Chilton, Didcot OX11 0QX, United Kingdom*
[5]*SUPA, Department of Physics, University of Strathclyde, 107 Rottenrow, Glasgow G4 0NG, United Kingdom*
[6]*Imperial College, The Blackett Laboratory, Imperial College London, London SW7 2AZ, United Kingdom*
[7]*AWE Plc., Aldermaston, Reading RG7 4PR, United Kingdom*
[8]*Department of Physics, Kohat University of Science and Technology, Kohat 26000, NWFP, Pakistan*
[9]*Nuclear Engineering Department, University of California–Berkeley, Berkeley, California 94709, USA*
[10]*Institut für Kernphysik, Technische Universität Darmstadt, Schloßgartenstrasse 9, D-64289 Darmstadt, Germany*
[11]*Department of Physics, University of York, Heslington, York YO10 5DD, United Kingdom*
[12]*School of Mathematics and Physics, Queen's University of Belfast, Belfast BT7 1NN, United Kingdom*

We have studied the dynamics of warm dense Li with near-elastic x-ray scattering. Li foils were heated and compressed using shock waves driven by 4-ns-long laser pulses. Separate 1-ns-long laser pulses were used to generate a bright source of 2.96 keV Cl Ly-α photons for x-ray scattering, and the spectrum of scattered photons was recorded at a scattering angle of 120° using a highly oriented pyrolytic graphite crystal operated in the von Hamos geometry. A variable delay between the heater and backlighter laser beams measured the scattering time evolution. Comparison with radiation-hydrodynamics simulations shows that the plasma is highly coupled during the first several nanoseconds, then relaxes to a moderate coupling state at later times. Near-elastic scattering amplitudes have been successfully simulated using the screened one-component plasma model. Our main finding is that the near-elastic scattering amplitudes are quite sensitive to the mean ionization state $\bar{Z}$ and by extension to the choice of ionization model in the radiation-hydrodynamics simulations used to predict plasma properties within the shocked Li.

I. INTRODUCTION

Warm dense matter (WDM) is a complex state of matter found between cold-condensed materials and hot dense plasmas that is the subject of considerable interest because of its relevance to astrophysics and inertial confinement fusion [1,2]. WDM is a strongly interacting quantum system defined by temperatures of a few electron volts and near solid densities [3,4], typically created in the laboratory as plasma heated by either an optical or free-electron laser [5]. A powerful diagnostic for WDM is x-ray scattering, whereby x-ray photons with wavelengths on the order of the plasma screening length reveal details of the plasma state [6].

Recent x-ray scattering studies at both large [7–10] and intermediate-scale [11] laser facilities have measured the fundamental plasma properties of temperature, ionization state, and density. Backward scattering spectra show the Compton feature [9], while plasmons, i.e., collective density oscillations, are observed in forward scattering [8]. Plasmons provide particularly robust measurements of the free-electron density [12] and temperature [13]. Other studies have used x-ray scattering to infer ionic structure and correlations [14–19], diagnose strong coupling [20] in WDM, and study bound-free contributions to scattering cross sections [21]. All of these studies highlight the broad applicability of x-ray scattering as a technique for diagnosing dense matter.

For lower-Z WDM plasmas with average ionization states $\bar{Z} \lesssim 1$, the x-ray scattering spectrum is dominated by the coherent (i.e., near-elastic) scattering from tightly bound electrons and electrons that are correlated with the ion motion, provided that the Compton shift energy is less than the binding energy of the inner-shell electrons. The intensity of the near-elastic scattering is described by the dynamic ion-ion structure factor $S_{ii}(k,\omega)$, where k is the magnitude of the scattering wave vector and ω is the probe photon frequency.

In this work, we used x-ray scattering to study the dynamics of lithium in the WDM regime. Two counterpropagating laser-driven shocks heated and compressed a solid Li foil, creating plasma conditions with temperatures $T_e \approx T_i \approx 2.0$ eV and density $\rho/\rho_0 \approx 2$. The dimensionless ion coupling parameter $\Gamma_{ii} = e^2 Z^2 / 4\pi\epsilon_0 k_B T_i (4\pi n_i/3)^{1/3} \approx 5$, indicative of a strongly coupled plasma [3,22]. Here, Z is the average ionic charge, $k_B T_i$ is the average ion temperature, and n_i is the average ionic density. We used the one-dimensional radiation-magnetohydrodynamics codes HELIOS-CR [23] and HYADES [24] to simulate the dynamic evolution of the laser-produced plasma, and in combination with the screened one-component plasma model (SOCP) [25,26] they produced results for the temporal evolution of the elastic scattering intensity that are consistent with the experimental data.

In contrast with previous work [17] that focused on studying the angular (wave vector k) dependence of the elastic

x-ray scattering, we have instead focused on the time dependence and on rigorous validation of the radiation-hydrodynamic simulation results. These simulation results have been validated by studying their sensitivity to the choice of radiation-hydrodynamic code (including the choice of the equation of state and ionization model), variations in temperature and ionization state, and plasma models.

Unlike previous work (on shocked Al) with near-elastic x-ray scattering [27], we do not observe a suppression of the elastic scattering signal early in time. This is due to the lower degree of coupling in this work ($\Gamma_{ii} \approx 5$ vs $\Gamma_{ii} \approx 240$) that is well below the crystallization point predicted for one-component plasmas with $\Gamma \gtrsim 125$ [28,29].

An important consideration is that near-elastic scattering is readily achieved at intermediate-scale laser facilities. Conversely, the requirements for inelastic scattering have only recently been demonstrated on such facilities by using a petawatt-class laser with Ti $K\alpha$ x rays [11]. Even with lower drive energy, near-elastic scattering is strong enough to validate modeling of the structure factor that goes into the SOCP model, providing a more easily obtained system for the study of x-ray scattering. Additionally, near-elastic scattering signals contain information on the spatial structure [25] and equation of state [30] of the system.

II. EXPERIMENTAL SETUP

We employed the eight-beam 527-nm-wavelength (2ω) Vulcan laser in the Target Area East at Rutherford Appleton Laboratory's Central Laser Facility [31]. As seen in Figs. 1(a) and 1(b), the scattering target consisted of a 50-μm-thick Li foil heated and compressed from opposing sides by two of the beams at 45° incidence. Each individual 50 J heater beam was used with a phase zone plate (PZP) [32] to achieve moderate uniform intensity on target. The PZP had an intrinsic focal spot diameter of 500 μm. To further lower the intensity, we increased the focal spot diameter to 650 μm by defocusing the beam. With a square-shaped pulse duration of 4 ns full width at half maximum (FWHM), the heater beam intensity was 3.8×10^{12} W/cm^2 when measured perpendicular to the beam axis. At the 45° angle of incidence, the on-target intensity was 2.7×10^{12} W/cm^2. The heating pulse had 0.3 ns rise and fall times, measured from 10% to 90% of the peak intensity.

To generate a bright source of the 2.96 keV Cl Ly-α x rays that were used to probe the Li plasma, the remaining six Vulcan beams irradiated a 5-μm-thick chlorine-containing parylene-D plastic foil with 300 J (i.e., 50 J per beam) in a 1 ns pulse. With a focal spot diameter of 50 μm, the overlaid backlighter laser intensity was 1.5×10^{16} W/cm^2. The resulting x ray yield was measured to be 7×10^{11} Ly-α photons per joule of laser energy into 4π (conversion efficiency 3.4×10^{-4}), within the range previously measured by other studies [6]. The backlighter beams were synchronized with the longer heater beams to 30 ps accuracy using a Hamamatsu streak camera and fired with a variable delay 2 ns $\leq \Delta t \leq 8$ ns (where Δt is the time between the rise of the heater pulses and the center of the backlighter pulses) to probe various time points during the temporal evolution of
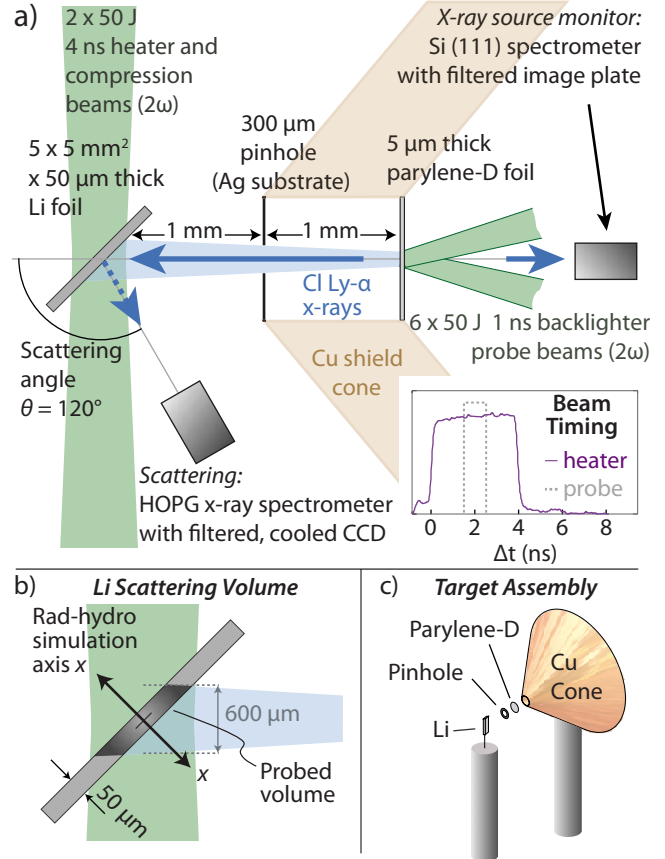

FIG. 1. (Color online) Experimental setup showing the x-ray scattering geometry and laser-target configuration. A 1 ns Cl Ly-α x-ray probe was generated by laser irradiation of a parylene-D plastic foil. The probe x-rays scattered off a Li target that was compressed by dual 4 ns laser beams and were then detected by the scattering spectrometer. Inset: laser beam timing diagram. The backlighter probe beam delay $\Delta t = t - t_0$, where t is the time at the center of the backlighter beams and t_0 is the time at the rise of the heater beam pulses.

the Li plasma. A Cu shield cone tipped with a 300-μm-diameter circular pinhole cut into an Ag substrate [see Fig. 1(c)] limited the Cl Ly-α x-ray illumination of the Li scattering target to a 600-μm-diameter region. The x-ray probed surface area was smaller than the region driven by the shock drive beams and, therefore, all scattered probe x rays came from uniformly shocked Li within the scattering volume shown in Fig. 1(b). Alignment of the Li scattering target and parylene-D backlighter foil was achieved to within 50 μm accuracy using a kinematic target mount and reference wires (not shown in Fig. 1).

Our main diagnostics consisted of x-ray spectrometers observing both the Li target and the primary x-ray source. The scattering spectrometer was a high-reflectivity highly oriented pyrolytic graphite (HOPG) [33] crystal, cylindrically bent with a radius of curvature of 107 mm and used in the von Hamos [34,35] geometry. The HOPG crystal had intraplane spacing $2d = 0.67$ nm, a mosaic spread of 0.8°, and an integrated reflectivity $R_{int} = 3.0 \pm 10\%$ mrad [36]. The spectrometer was aligned with a central energy of 2.96 keV, corresponding to a Bragg angle of 43.1° and a source to

crystal distance in the von Hamos geometry of $170 \pm 5\%$ mm [35]. In this configuration, the energy dispersion at the cooled Andor charge-coupled (CCD) detector was $dE/dx = 11.8$ eV/mm. The absolute energy resolution of the spectrometer was limited by broadening effects inherent to the crystal (i.e., depth broadening, roughness broadening, and mosaic broadening [35,36]) and the 25^2 μm^2 pixel size of the CCD camera. Neglecting source broadening from a finite-size plasma, the minimum instrument function width of the von Hamos spectrometer is estimated to be 1.1 eV, for a resolution at 2.96 keV of $\Delta E/E = 3.8 \times 10^{-4}$.

During the scattering experiments, source monitoring was achieved with a Si (111) flat crystal that viewed the source directly (cf. Fig. 1) and dispersed the x rays onto an absolutely calibrated Fuji BAS-SR image plate detector [37,38]. The integrated reflectivity of the Si (111) crystal was $R_{int} = 0.4 \pm 10\%$ mrad [39].

Filters were placed in front of the x-ray spectrometer detectors to attenuate the x rays and block visible light. For the scattering spectrometer, the filters consisted of 25 μm mylar and 25 μm Be, resulting in a filter transmission of $\tau_F(h\nu = 2.96$ keV$) = 0.56 \pm 5\%$. The source monitor spectrometer was filtered with 30 μm mylar overcoated with 100 nm Al for optical opacity, again yielding $\tau_F(h\nu = 2.96$ keV$) = 0.56 \pm 5\%$. These filters remained the same for all scattering data presented in this work.

The scattering and source spectrometer throughput efficiencies η_{scatt} and η_{source}, respectively, are defined as

$$\eta = \tau_F \frac{(R_{int} w/d)}{4\pi}. \tag{1}$$

The distances w and d are specific to the spectrometer geometry and will be defined momentarily; τ_F and R_{int} are the same as defined above. In the case of the scattering spectrometer, the von Hamos geometry focuses photons in the nondispersive direction, meaning that the size of the crystal in this direction is a limiting factor for the collection solid angle. Therefore, in the von Hamos geometry, w is the width of the crystal in the nondispersive direction and d is the source to *crystal* distance. With the flat crystal geometry source spectrometer, there is no focusing, and as a result w is the width of the illuminated portion of the detector and d is the source to *detector* distance. In this work, $\eta_{scatt} = 4.1 \times 10^{-5} \pm 13\%$ and $\eta_{source} = 3.8 \times 10^{-7} \pm 13\%$, where the propagated uncertainties have been estimated assuming no cross correlation. Another relevant factor is the throughput efficiency of the pinhole between the x-ray source and the Li target $\eta_{pinhole} = r^2/(4\pi d_{ph}^2)$, where r is the pinhole radius and d_{ph} is the source to pinhole distance. Our geometry as seen in Fig. 1 used a relatively large (1 mm $\pm 5\%$) distance from the x-ray source to the pinhole, resulting in $\eta_{pinhole} = 5.6 \times 10^{-3} \pm 10\%$. Larger distances can reduce the noise from the source plasma that is observed in the scattering spectra. A smaller distance (e.g., 0.5 mm) would have increased the brightness of the x-ray scattering source at the Li scattering target and will be applied in the future for study of the inelastic scattering in addition to the near-elastic scattering.

A calibration spectrum was taken by shooting a parylene-D foil that was placed at the position of the Li target. This provided an absolute calibration of the photon number and a calibration of the wavelength scale for the x-ray spectrometers. The total propagated systematic error in the measurements will be discussed in Sec. V.

III. RADIATION-HYDRODYNAMIC SIMULATIONS

The laser-target interaction and subsequent plasma conditions within the entire Li foil were calculated with the one-dimensional HELIOS-CR radiation-hydrodynamics code [23] and the PROPACEOS [23] equation of state (EOS). Ionization was simulated using a multigroup ionization model based on the quotidian equation of state (QEOS) [40] for strongly coupled plasmas. We also compared the results from HELIOS with one-dimensional simulations from the HYADES [24] radiation-hydrodynamics code with the SESAME [41] EOS and an average-atom local thermodynamic equilibrium ionization model. Both codes used the measured heater beam pulse profile (intensity 2.7 TW/cm² incident at 45°) as a simulation input. For brevity, these two simulation configurations will be referred to from now on as simply HELIOS and HYADES, with the understanding that the simulation code, EOS, and ionization model all contribute to the simulation results.

The predicted plasma conditions in the warm dense Li, as simulated by both HELIOS and HYADES, are shown in Fig. 2. HYADES simulations predict a lower mean ionization state $\bar{Z}$ in the densest regions of the plasma, likely due to the different ionization model. Nevertheless, within the experimental error bar, near-elastic scattering intensities simulated using the results of either code are consistent with our measurements.

Simulations using the hydrodynamic code H2D, a two-dimensional version of HYADES, confirm the one-dimensional nature of the interaction due to the large and uniform heater beam-spot size. Within the scattering volume, the predicted target compression varies by less than 5% between the one- and two-dimensional simulations. With HELIOS, we simulated each half of the Li foil separately using one heater beam and a fixed boundary condition at the center. This results in a single shock wave that reflects from the fixed boundary and mimics the counterpropagating shock wave conditions of the experiment. HYADES simulations used dual heater beams to produce true counterpropagating shocks, but this change in simulation geometry causes only a negligible impact on near-elastic scattering signals. Using HYADES, we simulated both a single reflecting shock and dual counterpropagating shocks and found that the predicted near-elastic scattering intensities vary by only 5% between the two cases.

During shock compression, HELIOS predicts a Li mass density of typically just over 1 g/cm³, a factor of 2 higher than solid density, at a pressure of approximately 1.6 Mbar. The shock velocity is 22 km/s calculated by observing the progression of the shock front at 0.25 ns intervals within the HELIOS simulations. Shock coalescence therefore begins at $\Delta t \approx 1.2$ ns.
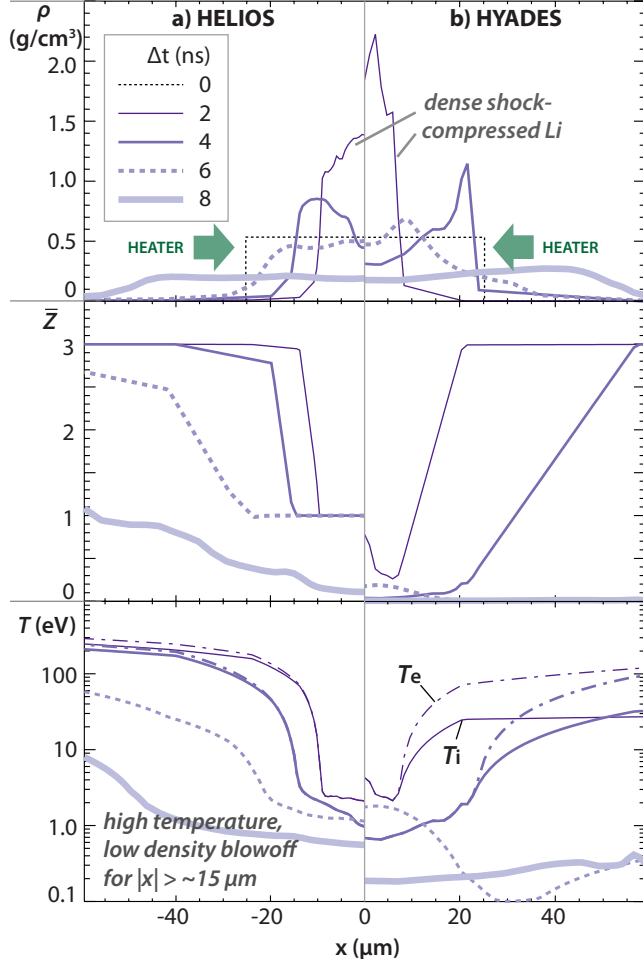
FIG. 2. (Color online) Plasma conditions in the warm dense Li, as simulated by the one-dimensional radiation-hydrodynamic codes (a) HELIOS-CR using the PROPACEOS equation of state with a multigroup ionization model based on the QEOS and (b) HYADES using the SESAME equation of state and an average-atom local thermodynamic equilibrium ionization model. x is the distance within the simulation, i.e., along the Li foil surface normal. The orientation of x and the scattering volume probed are shown in Fig. 1(b). Heater beam laser intensity was 2.7 TW/cm^2 incident at 45°.

IV. X-RAY SCATTERING THEORY

For small momentum transfers where the scattered photon frequency is close to the incident frequency, the magnitude of the scattering wave vector $\mathbf{k} = \mathbf{k}_0 - \mathbf{k}_1$ (the difference between the wave numbers of the scattered and incident radiation) is approximated [8] by the relation

$$k = |\mathbf{k}| = 4\pi \frac{E_0}{hc} \sin(\theta/2). \tag{2}$$

Our backscatter geometry had a probe photon energy of E_0 = 2.96 keV and a scattering angle θ = 120°, for a scattering vector magnitude of k = 2.6 Å^{-1}. It is worth noting that the binding energy for the second electron of neutral isolated Li (54.7 eV [42]) is greater than the Compton shift energy $\Delta E_C = \hbar^2 k^2/(2m_e)$ = 25 eV that is determined by the choice of k. As a result, there will be near-elastic scattering from

bound electrons. This can be an important factor to consider when designing an x-ray scattering experiment.

The effective screening length λ_s of a dense plasma is given by interpolation between the Debye length and the Thomas-Fermi length, i.e., between the classical and Fermi-degenerate regimes [6]. One approach [43] for calculating this effective screening length is to replace the electron temperature in the expression for the classical Debye length with a corrected temperature T_{cf}, giving $\lambda_s \approx (\epsilon_0 k T_{cf}/n_e e^2)^{1/2}$. To obtain T_{cf}, we consider a classical Coulomb fluid at an effective temperature $T_q = T_F(1.3251 - 0.1779\sqrt{r_s})$, where T_F is the Fermi temperature and r_s is the Wigner-Seitz radius. The effective temperature is then calculated as $T_{cf} = (T_e^2 + T_q^2)^{1/2}$, an approach that has been shown to be valid for arbitrary degeneracy [44]. For typical plasma conditions in the Li, the effective temperature T_{cf} is between 4.4 and 7.8 eV. The scattering parameter $\alpha = 1/k\lambda_s$ is then calculated to be between 0.49 and 0.58. This indicates that we studied the non-collective scattering regime, where $\alpha < 1$ [45].

The scattered photon spectrum is given by the spectrum of electron-density fluctuations within the plasma. We follow a standard approach [6,25,43,46] and describe the double-differential scattering cross section per unit volume in terms of the dynamic structure factor,

$$\frac{d^2\sigma}{d\Omega d\omega} = \sigma_T \frac{k_1}{k_0} S(k,\omega), \tag{3}$$

where σ_T is the Thomson cross section and $S(k,\omega)$ is the *total dynamic structure factor*, defined as the time and space Fourier transform of the time-dependent electron-density pair-correlation function. $S(k,\omega)$ may be written as the sum of scattering contributions from those electrons which are correlated with the motion of the ions and those which move freely, corresponding with near-elastic and inelastic scatterings, respectively. The total dynamic structure factor that represents the properties of the scattered spectrum is

$$S(k,\omega) = [f_I(k) + q(k)]^2 S_{ii}(k,\omega) + Z_f S_{ee}^0(k,\omega)$$

$$+ Z_c \int \widetilde{S}_{ce}(k,\omega - \omega') S_s(k,\omega') d\omega'. \tag{4}$$

The first term in Eq. (4) contains the behavior of the near-elastic scattering from those electrons that dynamically follow the ion motion; our experiments studied such scattering. The contribution from tightly bound electrons is represented by the ion form factor $f_I(k)$ [25,26], and the screening cloud of free (and valence) electrons that surround the ion is represented by the screening function $q(k)$ [25,47]. $S_{ii}(k,\omega)$ is the ion-ion dynamic structure factor, i.e., the ion-ion density correlation function.

Given the limited spectral resolution of our HOPG scattering spectrometer ($\Delta E/E \approx 10^{-3}$) and the roughly 6 eV FWHM of the Ly-α probe, the strong frequency dependence of $S_{ii}(k,\omega)$ is lost after convolution with the source profile and the spectrometer's instrument function. Consequently, the focus of our analysis shifts to the frequency-integrated static structure factor $(f_I + q)^2 S_{ii}(k)$, a quantity that determines the total measured near-elastic scattering signal. Physically, $S_{ii}(k)$ contains information on the spatial ordered-
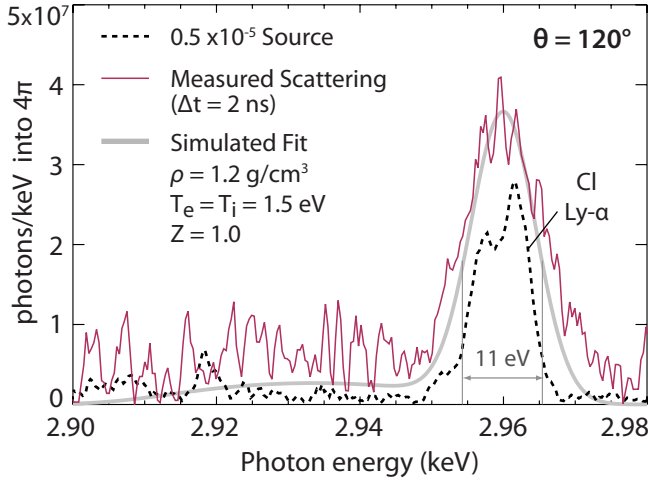
FIG. 3. (Color online) Measured (HOPG spectrometer) and simulated x-ray scattering spectra from shock-compressed Li for the Cl Ly-α doublet lines at $E_0=2.96$ keV. The strong near-elastic ion scattering feature is clearly visible. For comparison, the source spectrum (Si 111 spectrometer) is superimposed. The weak simulated signal centered near 2.93 keV consists of the inelastic free-electron feature. There is a possible systematic error of $\pm22\%$ and a random error of $\pm14\%$ in these absolute photon numbers.

ness of the system and is the Fourier transform of the pair-correlation function $g(r)$. When plotted as a function of k, $S_{ii}(k)$ can readily differentiate between less-ordered (e.g., liquid) and more-ordered (e.g., crystalline) states [25]. $S_{ii}(k)$ is important for determining the equation of state, and there is an analytic expression for the equation of state in terms of $S_{ii}(k)$ [30].

Terms two and three in Eq. (4) describe inelastic scattering behavior. Z_f and Z_c are the number of kinematically free and core electrons, respectively, and the total atomic charge $Z_A=Z_f+Z_c$. The $Z_f S_{ee}^0$ term describes inelastic Compton scattering from free electrons that are decoupled from the ion motion. Inelastic scattering can also occur when bound inner-core electrons are excited by probe photons to continuum states within the atom, resulting in a Raman-band-type spectrum. The properties of this bound-free scattering spectrum are described by the continuum of core electrons within an ion $\widetilde{S}_{ce}(k,\omega)$ modulated by the self-motion of the ions, represented by $S_s(k,\omega)$. In the high-frequency limit, $S_s(k,\omega)\approx\delta(\omega)$ [48].

In this study, the inelastic scattering features are small relative to the near-elastic scattering feature due to the scattering geometry, plasma conditions, and the atomic energy levels of Li. For $Z_f=1$ and $T_e\approx T_i\approx 2$ eV, the frequency-integrated total structure factor $S(k=2.6$ Å$^{-1})$ consists of 75% near-elastic scattering, 18% free-electron inelastic scattering, and 7% bound-free inelastic scattering. The relative scattering intensities are determined by the population level kinetics of the system. Assuming that the plasma is in local thermodynamic equilibrium, very simplified transition probabilities would include a Boltzmann scaling factor of $\exp[-\Delta E_\nu/k_B T]$, where ΔE_ν is the energy difference between the incoming and scattered photons. Bound-free transitions are only energetically permitted when the energy transferred

from the photon to the electron is greater than the energy of the bound state, meaning that the bound-free dynamic structure has cutoffs at the K and L-shell ionization energies. With $Z_f=1$, i.e., Li^{1+}, bound-free scattering therefore requires that $\Delta E_\nu>76$ eV, the K-shell ionization energy. Upon comparing with $\Delta E_\nu\approx0$ for near-elastic scattering and $\Delta E_\nu=\Delta E_C=25$ eV for free-electron inelastic (Compton) scattering, it becomes apparent that the relative intensity of both types of inelastic scattering is strongly suppressed by the higher-energy differences that enter into the Boltzmann factor. It should be noted that in higher-Z materials, such as carbon, L-shell bound-free scattering (where ΔE_ν is relatively small) has been shown to contribute significantly to the scattering spectrum [49]. For a much more detailed discussion of the inelastic scattering intensities, we refer the reader to Refs. [43,49].

In order to simulate the near-elastic scattering signals for our experiment, let us consider the power dP_s scattered into the frequency interval $d\omega$ and solid angle $d\Omega$ by power P_0 incident on a slab of scatterer density n and thickness dx. In terms of Eq. (3), we have

$$dP_s = P_0 n(x)dx \int \frac{d^2\sigma}{d\Omega d\omega}d\Omega d\omega$$

$$= P_0 \sigma_T \frac{k_1}{k_0}n(x)dx \int S(k,\omega)d\Omega d\omega. \quad (5)$$

In the small momentum-transfer limit, $k_1/k_0=1$. Since we are focusing on the near-elastic scattering signal from the ions, the structure factor $S(k,\omega)$ reduces to the ion structure term $(f_I+q)^2 S_{ii}(k,\omega)$ from Eq. (4). As there are temperature and density gradients within the plasma, we add explicit dependence on the spatial coordinate x to the ion form factor f, the screening function q, and the form factor S_{ii}, all of which depend on the plasma parameters. After integrating over frequency and solid angle, the total scattering power is finally calculated from Eq. (5) as a sum along x,

$$P_s = P_0 \sigma_T \sum n_i(x)[f_I(k,x) + q(k,x)]^2 S_{ii}(k,x)\Delta x, \quad (6)$$

where Δx is the width of the radiation-hydrodynamic simulation zones. The quantity $n_i(f_I+q)^2$ is the ion-motion correlated electron density, i.e., the electron density that actually contributes to the near-elastic scattering.

V. RESULTS AND DISCUSSION

Figure 3 shows a measured x-ray scattering spectrum with an elastically scattered ion feature at the incident x-ray energy of 2.96 keV. The bandwidth of this elastic scattering feature is 11 eV. The intrinsic width of the Ly-α source is approximately 6 eV, with the remaining bandwidth from the instrument function of the von Hamos scattering spectrometer, as discussed in Sec. II, as well as due to source broadening from a finite backlighter plasma size. Consistent with the low ionization states in this experiment, the inelastic free-electron scattering feature is weak. It is visible in the simulated spectrum in Fig. 3, downshifted by the 25 eV Compton shift near 2.93 keV, and cannot be quantitatively analyzed due to noise.

Plasma parameters from the HELIOS simulations were used with the SOCP model to fit the simulated x-ray scattering spectrum, as shown in Fig. 3. The scattering efficiency of the plasma is somewhat less than 10^{-5}, as can be seen by comparing the plotted source and measured intensities.

The key photometric figure of merit in this work is the ratio of the total (frequency-integrated) near-elastically scattered power to the incident power of the probe x rays. Using the pinhole and spectrometer throughputs defined earlier, and detector calibration factors C_{CCD} and C_{IP}, we have

$$\frac{P_s}{P_0} = \frac{\Sigma N_{scatt}(\omega)\Delta\omega}{\Sigma N_{source}(\omega)\Delta\omega} \frac{C_{CCD}/\eta_{scatt}}{C_{IP}\eta_{pinhole}/\eta_{source}}, \quad (7)$$

where $N_{scatt}(\omega)$ and $N_{source}(\omega)$ represent the net signal [number of CCD counts or amount of image plate photostimulated luminescence (PSL)] at the scattering and source detectors, respectively, into the frequency interval $\Delta\omega$. The detector calibration factors C_{CCD} and C_{IP} are determined by the quantum efficiency and gain for the CCD camera and by photons per PSL [37,38] (and to a small extent fading time) for the image plate.

Systematic error in the absolute photon calibration, i.e., the right-hand portion of Eq. (7), propagates from uncertainty in the spectrometer and pinhole throughput efficiencies, as discussed in Sec. II, as well as the detector calibration factors. To estimate the total systematic error in P_s/P_0, we assume that all uncertainties are uncorrelated and that both C_{CCD} and C_{IP} have an uncertainty of $\pm 5\%$. The total systematic error in P_s/P_0 is therefore approximately $\pm 22\%$. Calibration shots with parylene-D foils placed at the position of the Li target verified the value of the right-hand portion of Eq. (7) within this systematic error.

The frequency-integrated net signal $\Sigma N(\omega)\Delta\omega$ was calculated from the raw x-ray spectrometer data using the following procedure. First, a two-dimensional region of interest (ROI) was defined as the area containing the scattering signal within the captured spectrometer exposure. This subimage was smoothed with an average nearest-neighbor kernel to reduce noise, as shown in Fig. 4(a) for the scattering spectrometer. Second, pixel lineout profiles were calculated for each row of pixels in the subimage. A Gaussian scattering peak plus a locally linear background was fitted to each lineout using nonlinear least-squares curve fitting [50]. The background varied somewhat from lineout to lineout due to shot-to-shot noise conditions as well as imperfect von Hamos geometry imaging, in the case of the scattering spectrometer. Realistic constraints on the fit parameters (peak height and width greater than zero, peak width less than 15 eV) made the fitting process robust. Third, the background was subtracted to yield $N(\omega)$ shown in Fig. 4(b) for the scattering signal. Finally, the net signal in each lineout was summed to provide the total frequency-integrated net signal.

For warm Li scattering spectrometer exposures, the spectral range used for curve fitting included the weak inelastic signal. Since spectral noise and the weak inelastic signal are of similar strength, for this analysis we will consider the inelastic signal as merely another source of noise. We note that the fitted peak height depends on the background level, the value of which has an uncertainty determined by the

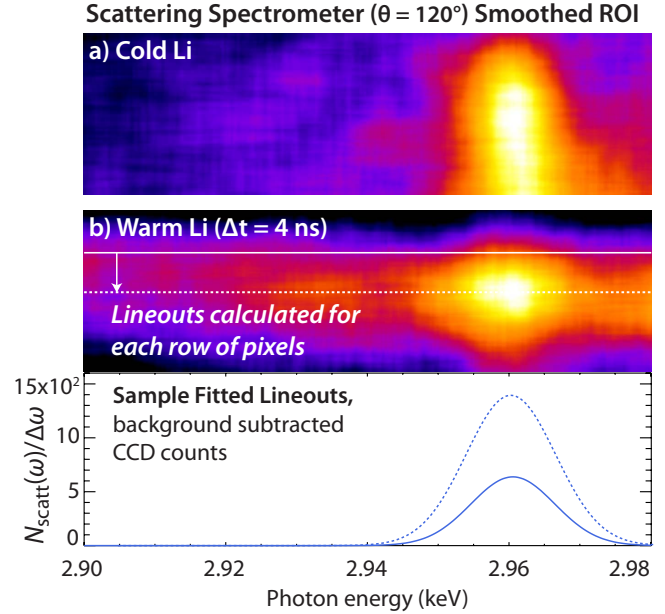**Scattering Spectrometer (θ = 120°) Smoothed ROI**

FIG. 4. (Color online) Smoothed ROI cropped from von Hamos scattering spectrometer exposures. (a) Cold Li x-ray scattering signal. (b) Illustration of the procedure used to determine the net scattering signal $N_{scatt}(\omega)$ from the warm laser-shocked Li with a probe delay $\Delta t = 4$ ns. Sample fitted lineouts are shown for the warm scattering; these were selected from the series of lineouts that was calculated for each row of pixels in the ROI. The frequency-integrated net signal is the sum $\Sigma N(\omega)\Delta\omega$ over all such lineouts from the ROI. Lineout height varies in the nondispersive (vertical) direction due to imperfect von Hamos geometry focusing.

noise. A characteristic measure of this uncertainty is the relative noise amplitude, defined to be the median amplitude of the noise divided by the height of the near-elastic signal. Uncertainty due to noise in the near-elastic scattering signals, as quantified by the relative noise amplitude averaged over all lineouts from a given ROI, is $\pm 10\%$ on average. This random error ranges from $\pm 5-30\%$, depending on the shot-to-shot noise levels in the scattering spectra.

Although the energies of the two heater beams E_1 and E_2 were nominally 50 J each, there was always some variation in the beam energy that caused an energy imbalance, defined as $|E_1 - E_2|/E_1$. The average energy imbalance was 22%. To ensure that relatively consistent hydrodynamic conditions existed in the Li from shot to shot, we rejected all data points with a heater beam energy imbalance greater than 30%. Simulations with HELIOS indicate that such a variation in heater beam energy corresponds to an uncertainty of $\pm 7\%$ in the total elastic scattering signals.

Random error from all sources, represented in the data error bars plotted on Fig. 5, is due to noise in the spectra and variation in the heater beam energy (ordinate) and the x-ray backlighter pulse length (abscissa). The gray shaded region in Fig. 5 shows the average measured value of the near-elastic scattering intensity, bounded by the average ordinate error bar at each time point. This average error bar has been scaled down by a factor of $\sqrt{n}$, where n is the sample size, to reflect greater confidence in those measurements with a larger sample size.
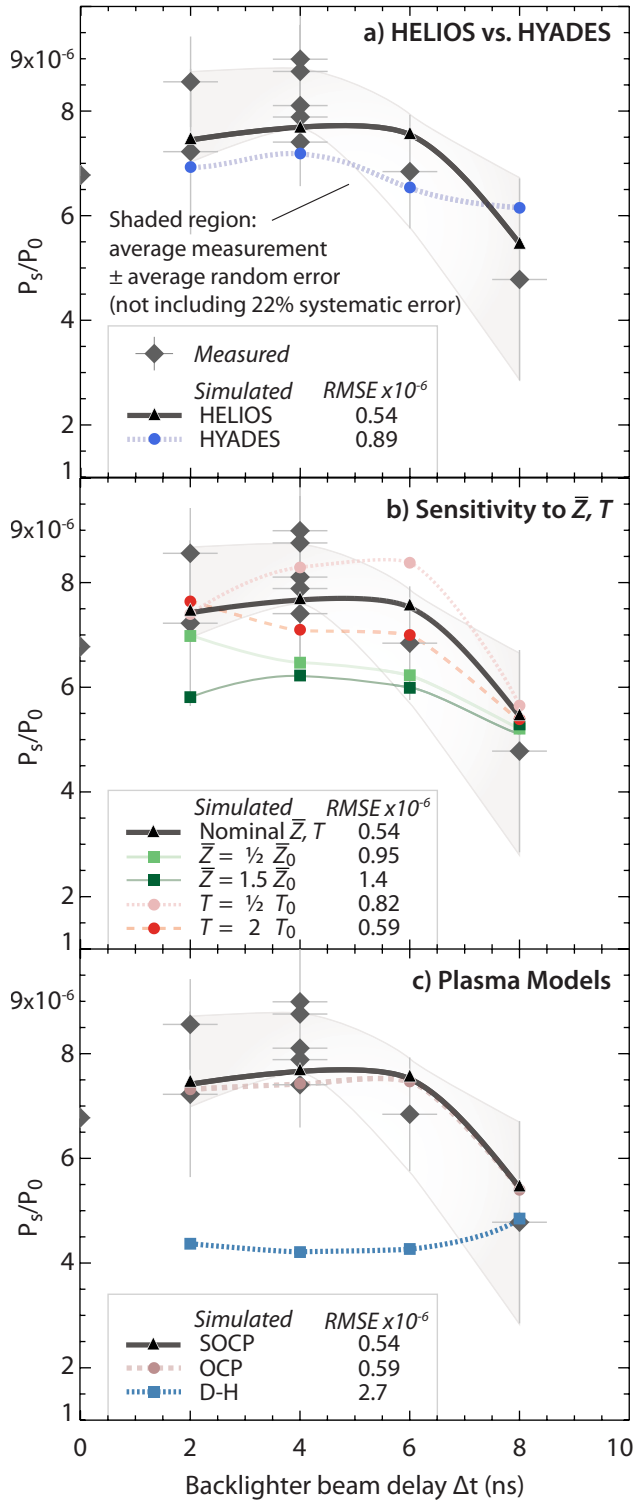
FIG. 5. (Color online) Time evolution of the total frequency-integrated near-elastic scattering intensity, both measured and simulated. (a) Comparison of HELIOS and HYADES simulations using the SOCP model. (b) Sensitivity to variations in plasma mean ionization state $\bar{Z}$ and temperature T, using HELIOS simulation results and the SOCP model. (c) Comparison of plasma models: SOCP, unscreened OCP, and Debye-Hückel (D-H). Quality of fit is quantified by the average RMSE. The measured data points at $\Delta t = 0$ represent the cold scatter level from unheated Li.

For 1-ns-long backlighter laser pulses, as used in this work, the Cl Ly-α x-ray emission time is on the order of the laser-pulse length [51,52]. There is also a small jitter (not studied in this work) that is associated with the beam timing and introduces a small uncertainty to the starting time of the x-ray backlight. Consequently, the measured scattering signals in Fig. 5 have an abscissa error bar extending 0.5 ns before and after the nominal delay time Δt.

Cold data points shown in Fig. 5 at $\Delta t = 0$ represent the near-elastic x-ray scattering from unheated Li. The measured scattering signal was obtained by firing only the backlighter beams and not the heater beams.

The simulated near-elastic scattering signals shown in Fig. 5 were calculated from Eq. (6). The ion density n_i is from the radiation-hydrodynamic simulations; f_I, q, and $S_{ii}(k)$ were calculated using the SOCP model (using the plasma parameters also from the simulations at each point x). This method takes into account the inhomogeneity and gradients in the scattering plasma. The quality of fit for the various simulated scattering signals is quantified by the average root mean-squared error (RMSE) between the measured and simulated data points. Perfect agreement between the data sets would be indicated by a RMSE of zero.

Figure 5 is organized into three parts as follows. Part (a) compares the predictions of the HELIOS and HYADES radiation-hydrodynamic simulations (and the choice of EOS and ionization balance model used with each code). Part (b) shows the results of a sensitivity study that varied input temperature and ionization state, and part (c) compares the predictions of various plasma models. The simulated scattering signals shown in parts (a) and (b) were calculated using the SOCP model.

As seen in Fig. 5(a), near-elastic scattering signals simulated using plasma parameters from either the HELIOS or HYADES radiation-hydrodynamic codes are generally consistent with the measured data. The HELIOS results more closely match the average measured scattering signal, which led us to preferentially use HELIOS in this work. Again, we note that the combination of simulation code, EOS, and ionization model gives these results. Previously, consistent results between the PROPACEOS and SESAME equations of state have been achieved using HELIOS [53]. This suggests that the discrepancy we observe might be due to the choice of ionization model rather than the choice of EOS.

A sensitivity study was performed to assess which plasma parameters most strongly influence the total near-elastic scattering; the results of this study are shown in Fig. 5(b). Four test cases were utilized, wherein the input temperature was changed to (1) half the nominal value predicted by HELIOS and (2) twice the nominal value, the mean ionization state was changed to (3) half the nominal value, and (4) 1.5 times the nominal value. Meanwhile, all other plasma parameters remained unchanged. These test cases were used to calculate the simulated total near-elastic scattering with the SOCP theory. The results of this sensitivity study indicate that the total predicted near-elastic scattering is quite sensitive to variations in ionization state and somewhat sensitive to variations in temperature.

Indeed, the main finding of this work is that the near-elastic scattering intensity is quite sensitive to the plasma

TABLE I. Sensitivity of the near-elastic scattering parameters in warm dense Li to variation in the mean ionization state used in the SOCP model. Nominal mass density, mean ionization state, and temperature (ion and electron) predicted by HELIOS for the simulation zone at $x=10$ μm are ρ, $\bar{Z}$, and T, for $\Delta t=4$ ns. The total near-elastic scattering intensity is determined by the total ion structure factor S_i.

ρ (g/cm^3)	T_i (eV)	T_e (eV)		f	q	S_{ii}	S_i
0.85	2.1	2.1	$\bar{Z}=\frac{1}{2}\overline{Z_0}=0.5$	1.78	0.10	0.91	3.2
0.85	2.1	2.1	$\bar{Z}=\overline{Z_0}=1.0$	1.78	0.29	0.92	4.0
0.85	2.1	2.1	$\bar{Z}=1.5\overline{Z_0}=1.5$	1.20	0.51	1.18	3.4

mean ionization state. At $\Delta t=4$ ns, changing the mean ionization state supplied to the SOCP model by a factor of 2 lower or 1.5 higher causes the simulated scattering intensity to fall significantly and no longer lie within the average measurement and error bar region.

This change in near-elastic scattering intensity can be understood by looking in more detail at the plasma and scattering parameters for one of the HELIOS radiation-hydrodynamic simulation zones (cf. Table I). At $x=10$ μm, the local mass density $\rho=0.85$ g/cm^3, temperature $T_i=T_e=2.1$ eV, and the nominal mean ionization state $\overline{Z_0}=1.0$. When these parameters are supplied to the SOCP model, the predicted ion form factor $f_I=1.78$, the screening function $q=0.29$, the ion structure factor $S_{ii}=0.92$, and the total ion structure factor $S_i=(f_I+q)^2 S_{ii}=4.0$. When we set $\bar{Z}=\frac{1}{2}\overline{Z_0}=0.5$ (while holding ρ and T constant), neither f_I nor S_{ii} changes appreciably but q drops by a factor of 3 to 0.10, causing S_i to fall to 3.2, a decrease of 18%. For this test case and all of the other test cases in this sensitivity study, the changing value of S_i is what directly determines the different scattering intensities shown in Fig. 5(b).

Let us consider in more detail this behavior of the scattering parameters at low ionization states. As $\bar{Z}$ decreases from 1 to 0.5, half of the singly ionized Li *ions* are replaced by neutral Li *atoms*. This means that the ion form factor is now partially replaced by the atomic form factor $f_A(k)$ [49]. Tabulated numerical fits [54] give $f_A(k=2.6$ Å$^{-1})=1.73$ for neutral Li, essentially the same as the ion form factor calculated in this work for $\bar{Z}=1$ and $\bar{Z}=0.5$. In other words, the ion form factor for Li is determined almost exclusively by the deeply bound 1s electrons, and the added presence of some 2s electrons from the neutral Li atoms does not contribute noticeably to the near-elastic scattering. As $\bar{Z}$ decreases from 1 to 0.5, the reduction in q is not matched by an increase in f_I and the total scattering intensity falls accordingly.

Similarly, with $\bar{Z}=0.5$ the ion structure factor S_{ii} is partially replaced by an equivalent structure factor for a neutral gas. In the Debye-Hückel model [55], valid for weakly coupled plasmas, $S(k)=k^2/(k^2+k_D^2)$. For a neutral gas, $k_D=0$ and therefore $S(k)=1$. Since $S_{ii}\approx 0.9$ is already very close to unity, the change in the structure factor is small and therefore has a minimal impact on the change in the total near-elastic scattering intensity.

Going in the other direction and increasing the ionization state, we now set $\bar{Z}=1.5\overline{Z_0}=1.5$, i.e., in addition to singly ionized Li, some Li ions are now doubly ionized. This means that there are fewer 1s bound electrons, causing f_I to drop to 1.2. Some of these electrons join the screening cloud and cause q to increase to 0.51, but nevertheless there is a net drop in $(f_I+q)^2$. Since the ion structure factor S_{ii} remains close to unity, the total ion structure factor $S_i=3.4$ is again lower than for $\bar{Z}=\overline{Z_0}$, as shown in Table I. In this case, S_i decreases by 14%.

As for the sensitivity of the near-elastic scattering to plasma temperature, we find that the predicted scattering intensity changes primarily due to different values of q. When $T_i\to 0.5T_i$ and $T_e\to 0.5T_e$, we have $q=0.31$ and $S_{ii}=0.97$, for a total ion structure factor $S_i=4.2$, an increase of about 7%. For $T_i\to 2T_i$ and $T_e\to 2T_e$, $q=0.25$, $S_{ii}=0.91$, and $S_i=3.7$, a decrease of about 5%.

For the relatively large scattering vector magnitude of $k=2.6$ Å^{-1} in this work, the effect of the electron-ion screening is minimal and there is little difference predicted between the screened and unscreened one-component plasma models [25]. As expected, for the near-elastic scattering time series we calculated almost identical results when using SOCP and OCP, as shown in Fig. 5(c). Within the measurement uncertainty, simulated scattering signals calculated using the SOCP model are the same as those calculated using the OCP model. By contrast, calculations using the Debye-Hückel model grossly underestimate the scattering intensity because this model is not valid in the strongly coupled regime. Very late in time, at $\Delta t=8$ ns, all three models start to converge as the plasma becomes less strongly coupled. The plasma parameters supplied to all three theoretical models were from the best-fit (heater intensity 2.7 TW/cm^2 incident at 45°) HELIOS radiation-hydrodynamic simulations.

The average values of the simulated static structure factor $S_{ii}(k)$, average ion density $\overline{n}_i$, ion temperature $\overline{T}_i$, the ion coupling parameter $\overline{\Gamma}_{ii}$, and the scattering parameter $\bar{\alpha}$ were calculated by integrating through the length of the Li foil and weighting to $n_i(f_I+q)^2$, the near-elastic scatterer density, i.e., the ion-motion correlated electron density. For example,

$$\overline{S_{ii}}(k) = \frac{\sum S_{ii}(k,x)n_i(x)[f_I(k,x)+q(k,x)]^2\Delta x}{\sum n_i(x)[f_I(k,x)+q(k,x)]^2\Delta x}. \tag{8}$$

The spatially integrated values for the plasma parameters are shown in Table II.

The plasma is highly coupled during the first few nanoseconds of the laser driver with $\Gamma_{ii}>1$. At later times, S_{ii} goes to 1, the value expected for an ideal plasma, and Γ_{ii}

TABLE II. Time evolution of average plasma parameters predicted by HELIOS simulations for counter-propagating shock-compressed Li, diagnosed with x-ray scattering at $\theta = 120°$. Shown are the averages for ion temperature $\overline{T_i}$, ion density $\overline{n_i}$, ionization state $\overline{Z}$, static structure factor $\overline{S_{ii}}(k = 2.6 \text{ Å}^{-1})$, ion-ion coupling parameter $\overline{\Gamma_{ii}}$, and scattering parameter $\overline{\alpha}$. S_{ii} was calculated using the SOCP model.

Δt (ns)	$\overline{T_i}$ (eV)	$\overline{n_i}$ (cm^{-3})	$\overline{Z}$	$\overline{S_{ii}(k)}$	$\overline{\Gamma_{ii}}$	$\overline{\alpha}$
2	2.6	1.1×10^{23}	1.0	0.81	4.7	0.59
4	2.4	6.3×10^{22}	1.0	0.98	5.0	0.52
6	2.0	3.7×10^{22}	1.0	1.07	5.3	0.46
8	1.2	1.6×10^{22}	0.5	1.00	1.5	0.31

falls as the plasma becomes less strongly coupled due to decreasing mean ionization state $\overline{Z}$ in the densest region of the plasma.

VI. CONCLUSIONS

We have successfully matched the time evolution of the static ion-ion structure factor in the screened one-component plasma model to experimental results for warm dense Li. Moreover, we have observed that the simulated near-elastic scattering amplitudes are quite sensitive to the mean ionization state $\overline{Z}$ and by extension to the choice of ionization model in the radiation-hydrodynamics simulations used to predict the plasma properties within the shocked Li. We observe that the results obtained using the HELIOS radiation-hydrodynamics code, the PROPACEOS equation of state, and a multigroup ionization model based on the QEOS are generally consistent with the measured data, as are results from the HYADES radiation-hydrodynamics code, the SESAME EOS, and an average-atom local thermodynamic equilibrium ionization model. In the future, we will extend this validation of simulation results to inelastic x-ray scattering.

[1] N. Nettelmann, B. Holst, A. Kietzmann, M. French, R. Redmer, and D. Blaschke, Astrophys. J. **683**, 1217 (2008).

[2] J. D. Lindl, P. Amendt, R. L. Berger, S. G. Glendinning, S. H. Glenzer, S. W. Haan, R. L. Kauffman, O. L. Landen, and L. J. Suter, Phys. Plasmas **11**, 339 (2004).

[3] S. Ichimaru, Rev. Mod. Phys. **54**, 1017 (1982).

[4] R. W. Lee, S. J. Moon, H. Chung, W. Rozmus, H. A. Baldis, G. Gregori, R. C. Cauble, O. L. Landen, J. S. Wark, A. Ng, S. J. Rose, C. L. Lewis, D. Riley, J. Gauthier, and P. Audebert, J. Opt. Soc. Am. B **20**, 770 (2003).

[5] U. Zastrau, C. Fortmann, R. R. Faustlin, L. F. Cao, T. Doppner, S. Dusterer, S. H. Glenzer, G. Gregori, T. Laarmann, H. J. Lee, A. Przystawik, P. Radcliffe, H. Reinholz, G. Ropke, R. Thiele, J. Tiggesbaumker, N. X. Truong, S. Toleikis, I. Uschmann, A. Wierling, T. Tschentscher, E. Forster, and R. Redmer, Phys. Rev. E **78**, 066406 (2008).

[6] S. Glenzer and R. Redmer, Rev. Mod. Phys. **81**, 1625 (2009).

[7] H. J. Lee, P. Neumayer, J. Castor, T. Doppner, R. W. Falcone, C. Fortmann, B. A. Hammel, A. L. Kritcher, O. L. Landen, R. W. Lee, D. D. Meyerhofer, D. H. Munro, R. Redmer, S. P. Regan, S. Weber, and S. H. Glenzer, Phys. Rev. Lett. **102**, 115001 (2009).

[8] S. H. Glenzer, O. L. Landen, P. Neumayer, R. W. Lee, K. Widmann, S. W. Pollaine, R. J. Wallace, G. Gregori, A. Höll, T. Bornath, R. Thiele, V. Schwarz, W. D. Kraeft, and R. Redmer, Phys. Rev. Lett. **98**, 065002 (2007).

[9] S. H. Glenzer, G. Gregori, R. W. Lee, F. J. Rogers, S. W. Pollaine, and O. L. Landen, Phys. Rev. Lett. **90**, 175002 (2003).

[10] G. Gregori, S. H. Glenzer, K. B. Fournier, K. M. Campbell, E. L. Dewald, O. S. Jones, J. H. Hammer, S. B. Hansen, R. J. Wallace, and O. L. Landen, Phys. Rev. Lett. **101**, 045003 (2008).

[11] A. L. Kritcher, P. Neumayer, J. Castor, T. Doppner, R. W. Falcone, O. L. Landen, H. J. Lee, R. W. Lee, E. C. Morse, A. Ng, S. Pollaine, D. Price, and S. H. Glenzer, Science Magazine **322**, 69 (2008).

[12] R. Thiele, T. Bornath, C. Fortmann, A. Höll, R. Redmer, H. Reinholz, G. Ropke, A. Wierling, S. H. Glenzer, and G. Gregori, Phys. Rev. E **78**, 026411 (2008).

[13] T. Döppner, O. Landen, H. Lee, P. Neumayer, S. Regan, and S. Glenzer, High Energy Density Phys. **5**, 182 (2009).

[14] K. Wunsch, J. Vorberger, and D. O. Gericke, Phys. Rev. E **79**, 010201(R) (2009).

[15] G. Gregori and D. O. Gericke, Phys. Plasmas **16**, 056306 (2009).

[16] B. Barbrel, M. Koenig, A. Benuzzi-Mounaix, E. Brambrink, C. R. D. Brown, D. O. Gericke, B. Nagler, M. Rabecle Gloahec, D. Riley, C. Spindloe, S. M. Vinko, J. Vorberger, J. Wark, K. Wunsch, and G. Gregori, Phys. Rev. Lett. **102**, 165004 (2009).

[17] E. García Saiz, G. Gregori, D. O. Gericke, J. Vorberger, B. Barbrel, R. J. Clarke, R. R. Freeman, S. H. Glenzer, F. Y. Khattak, M. Koenig, O. L. Landen, D. Neely, P. Neumayer, M. M. Notley, A. Pelka, D. Price, M. Roth, M. Schollmeier, C. Spindloe, R. L. Weber, L. van Woerkom, K. Wunsch, and D. Riley, Nat. Phys. **4**, 940 (2008).

[18] G. Gregori, S. H. Glenzer, and O. L. Landen, Phys. Rev. E **74**, 026402 (2006).

[19] D. Riley, N. C. Woolsey, D. McSherry, I. Weaver, A. Djaoui, and E. Nardi, Phys. Rev. Lett. **84**, 1704 (2000).

[20] D. Riley, I. Weaver, D. McSherry, M. Dunne, D. Neely, M. Notley, and E. Nardi, Phys. Rev. E **66**, 046408 (2002).

[21] D. Riley, F. Khattak, E. García Saiz, G. Gregori, S. Bandyopadhyay, M. Notley, D. Neely, D. Chambers, A. Moore, and A. Comley, Laser Part. Beams **25**, 465 (2007).

[22] S. G. Brush, H. L. Sahlin, and E. Teller, J. Chem. Phys. **45**, 2102 (1966).

[23] J. MacFarlane, I. Golovkin, and P. Woodruff, J. Quant. Spectrosc. Radiat. Transf. **99**, 381 (2006).

[24] J. T. Larsen and S. M. Lane, J. Quant. Spectrosc. Radiat. Transf. **51**, 179 (1994).

[25] G. Gregori, A. Ravasio, A. Höll, S. Glenzer, and S. Rose, High Energy Density Phys. **3**, 99 (2007).

[26] S. Galam and J. Hansen, Phys. Rev. A **14**, 816 (1976).

[27] A. Ravasio, G. Gregori, A. Benuzzi-Mounaix, J. Daligault, A. Delserieys, A. Y. Faenov, B. Loupias, N. Ozaki, M. Rabecle Gloahec, T. A. Pikuz, D. Riley, and M. Koenig, Phys. Rev. Lett. **99**, 135006 (2007).

[28] N. Itoh and S. Ichimaru, Phys. Rev. B **22**, 1459 (1980).

[29] R. C. Gann, S. Chakravarty, and G. V. Chester, Phys. Rev. B **20**, 326 (1979).

[30] M. Baus and J. Hansen, Phys. Rep. **59**, 1 (1980).

[31] I. Ross, M. White, J. Boon, D. Craddock, A. Damerell, R. Day, A. Gibson, P. Gottfeldt, D. Nicholas, and C. Reason, IEEE J. Quantum Electron. **17**, 1653 (1981).

[32] T. H. Bett, C. N. Danson, P. Jinks, D. A. Pepler, I. N. Ross, and R. M. Stevenson, Appl. Opt. **34**, 4025 (1995).

[33] H. Legall, H. Stiel, V. Arkadiev, and A. A. Bjeoumikhov, Opt. Express **14**, 4570 (2006).

[34] A. P. Shevelko, I. I. Sobelman, and V. A. Slemzin, *Current Russian Research in Optics and Photonics: New Methods and Instruments for Space- and Earth-based Spectroscopy in XUV, UV, IR, and Millimeter Waves* (SPIE, Russia, 1998), Vol. 3406, pp. 91–108.

[35] M. Urry, G. Gregori, O. Landen, A. Pak, and S. Glenzer, J. Quant. Spectrosc. Radiat. Transf. **99**, 636 (2006).

[36] A. Pak, G. Gregori, J. Knight, K. Campbell, D. Price, B. Ham-mel, O. L. Landen, and S. H. Glenzer, Rev. Sci. Instrum. **75**, 3747 (2004).

[37] A. L. Meadowcroft, C. D. Bentley, and E. N. Stott, Rev. Sci. Instrum. **79**, 113102 (2008).

[38] I. J. Paterson, R. J. Clarke, N. C. Woolsey, and G. Gregori, Meas. Sci. Technol. **19**, 095301 (2008).

[39] B. L. Henke, E. M. Gullikson, and J. C. Davis, At. Data Nucl. Data Tables **54**, 181 (1993).

[40] R. M. More, K. H. Warren, D. A. Young, and G. B. Zimmerman, Phys. Fluids **31**, 3059 (1988).

[41] SESAME: *The Los Alamos National Laboratory Equation of State Database*, edited by S. P. Lyon and J. D. Johnson (LANL, New Mexico, 1992); Report number LA-UR-92–3407.

[42] J. A. Bearden and A. F. Burr, Rev. Mod. Phys. **39**, 125 (1967).

[43] G. Gregori, S. H. Glenzer, W. Rozmus, R. W. Lee, and O. L. Landen, Phys. Rev. E **67**, 026412 (2003).

[44] F. Perrot and M. W. C. Dharma-wardana, Phys. Rev. B **62**, 16536 (2000).

[45] A. Kritcher, P. Neumayer, M. Urry, H. Robey, C. Niemann, O. Landen, E. Morse, and S. Glenzer, High Energy Density Phys. **3**, 156 (2007).

[46] H. Kunze and W. Lochte-Holtgreven, *Plasma Diagnostics* (North-Holland, Amsterdam, 1968).

[47] D. B. Boercker and R. M. More, Phys. Rev. A **33**, 1859 (1986).

[48] J. Hansen and I. McDonald, *Theory of Simple Liquids*, 3rd ed. (Academic, New York, 2006).

[49] G. Gregori, S. H. Glenzer, F. J. Rogers, S. M. Pollaine, O. L. Landen, C. Blancard, G. Faussurier, P. Renaudin, S. Kuhlbrodt, and R. Redmer, *45th Annual Meeting of the APS Division of Plasma Physics* (AIP, Albuquerque, New Mexico, 2004), Vol. 11, pp. 2754–2762.

[50] C. Markwardt, in Proceedings of ADASS XVIII, Quebec, ASP Conference Series, Vol. 411, edited by D. Bohlender, P. Dowler, and D. Durand (Astronomical Society of the Pacific, San Francisco, CA, 2009), p. 251.

[51] D. L. Matthews, E. M. Campbell, N. M. Ceglio, G. Hermes, R. Kauffman, L. Koppel, R. Lee, K. Manes, V. Rupert, V. W. Slivinsky, R. Turner, and F. Ze, J. Appl. Phys. **54**, 4260 (1983).

[52] R. Kauffman, in *Physics of Laser Plasma*, Handbook of Plasma Physics, edited by A. Rubenchik and S. Witkowski (North-Holland, Amsterdam, 1991), Vol. 3, p. 111.

[53] J. J. MacFarlane, Comparisons of HELIOS simulation results using PROPACEOS and SESAME equations of state (www.prism-cs.com).

[54] D. Waasmaier and A. Kirfel, Acta Crystallogr., Sect. A: Found. Crystallogr. **51**, 416 (1995).

[55] D. Salzmann, *Atomic Physics in Hot Plasmas* (Oxford University Press, New York, 1998).